Received: 7 June 2018 | Revised: 26 July 2018 | Accepted: 27 August 2018

DOI: 10.1111/ter.12358

PAPER

WILEY Terra Nova

Direct observation of dislocation nucleation in pyrite using combined electron channelling contrast imaging and electron backscatter diffraction

Anna Rogowitz[1] | Stefan Zaefferer[2] | Renelle Dubosq[3]

[1]Department of Geodynamics and Sedimentology, University of Vienna, Vienna, Austria

[2]Max Planck Institute for Iron Research, Dusseldorf, Germany

[3]Department of Earth & Environmental Sciences, University of Ottawa, Ottawa, ON, Canada

Correspondence
Anna Rogowitz, Department of Geodynamics and Sedimentology, University of Vienna, Vienna, Austria.
Email: anna.rogowitz@univie.ac.at

Funding information
Austrian Science Fund, Grant/Award Number: P 29539-N29

*The copyright line for this article was changed on 16 November 2018 after original online publication

Abstract

Crystal-plastic deformation is one of the main mechanisms that can accommodate large amounts of strain within the lithosphere. Despite the requirement of understanding dislocation nucleation and arrangement, the only accepted method for direct observation of dislocations in geological materials so far is transmission electron microscopy. Herein, we present a study using a combination of electron channelling contrast imaging (ECCI) and electron backscatter diffraction (EBSD) to visualize and analyse crystal defects in pyrite deforming close to the crystal plastic to brittle transition zone. Structures in focus include (a) dislocation nucleation at crack-tips and (b) the reactivation of mode I cracks accompanied by the nucleation of dislocations and crystal-plastic behaviour resulting in the development of complex dislocation structures and low-angle grain boundaries. EBSD maps reveal an increase in misorientation towards micro-cracks, consistent with a greater dislocation density along cracks observed by ECCI.

1 | INTRODUCTION

In geological materials, the presence and multiplication of dislocations is indispensable to accommodate larger amounts of strain by continuous creep processes, possibly controlling large-scale tectonic processes. To fully understand the deformation behaviour of the lithosphere, it is essential to analyse the nucleation, structure and arrangement of dislocations during deformation. New developments in electron backscatter diffraction (EBSD), namely high-angular resolution EBSD (HR-EBSD) based on pattern cross-correlation, allow for quantitative analysis of microstructures and dislocation densities down to a resolution of 0.05° (Wallis, Parsons, & Hansen, 2017; Wheeler et al., 2009). Nevertheless, the direct observation of crystal defects has been so far restricted to transmission electron microscopy (TEM), limiting observations to the size of a thin foil (Hirsch et al., 1960). In this study, we use electron channelling contrast imaging (ECCI), partly under controlled diffraction conditions, to analyse crystal defects in pyrite. ECCI uses backscatter electrons in high-resolution scanning electron microscopy, allowing direct observation of crystal defects with a contrast very similar to scanning transmission electron microscopy (STEM). The combined ECCI and EBSD approach allows the adjustment of proper diffraction conditions and a crystallographic interpretation of the defect contrast (Miyajima, Abeykoon, & Heidelbach, 2018; Zaefferer & Elhami, 2014).

Pyrite is a ubiquitous sulphide phase in ore deposits, and is of great interest for its incorporation of Au. Due to its crystallography, it is a relatively strong mineral assumed to mainly deform in a brittle manner. Nevertheless, crystal-plastic deformation of pyrite has been observed and has became the focus of various studies over the last years as it has been linked to the remobilization of Au (Boyle, Prior, Banham, & Timms, 1998; Dubosq, Lawley, Rogowitz, Schneider, & Jackson, 2018; Fougerouse, Micklethwaite et al., 2016; Fougerouse, Reddy et al., 2016). Dubosq et al. (2018) observed Au enrichment in pyrite micro-substructures (i.e. low-angle grain boundaries, micro-cracks), arguing such might act as Au-traps. Herein, we investigate

This is an open access article under the terms of the Creative Commons Attribution License, which permits use, distribution and reproduction in any medium, provided the original work is properly cited.
© 2018 The Authors. *Terra Nova* Published by John Wiley & Sons Ltd

the interaction of micro-cracking, dislocation nucleation and the onset of plastic deformation in pyrite samples from the Detour Lake mine (Canada) using a combination of EBSD and ECCI.

2 | GEOLOGICAL SETTING

The Detour Lake deposit is a Neoarchaean orogenic gold deposit located in the northernmost region of the Abitibi subprovince in Canada along the Sunday Lake Deformation Zone (SLDZ), which has undergone four major regional-scale deformation events (D_1–D_4; Oliver et al., 2011). Herein, we focus on structures related to D_2. Its penetrative foliation fabric, S_2, is defined by actinolite and biotite, which make up part of the lower amphibolite metamorphic mineral assemblage, suggesting peak metamorphic conditions of around 550°C and 3.3 kbar during D_2 (Marmont, 1987; Oliver et al., 2011). Inclusions of prograde metamorphic minerals in pre- to syn-D_2 mineralized veins are consistent with peak metamorphic conditions during D_2 (Dubosq et al., 2018; Oliver et al., 2011).

Although the exact hydrothermal events or processes that caused veining at the Detour Lake deposit remain poorly understood, we assume they are consistent with the orogenic gold deposit forming model proposed by Bleeker (2015). In this model, Bleeker suggests that the near-surface environment where Au deposition is concentrated has a high pressure and temperature gradient and a low confining pressure, which allow for the dilation and opening of vein systems. The inversion of the main fault zones, in this case, the SLDZ, from extensional to thrust creates an ideal deep-reaching fluid conduit for the advection of Au-bearing hydrothermal fluids (Bleeker, 2015).

3 | METHODS

Microstructures ranging from brittle to crystal-plastic behaviour have been investigated using a combination of EBSD and ECCI. Quantitative analysis of crystal distortion has been performed by EBSD mapping on a FEI Quanta 3D FEG instrument. The scanning electron microscope (SEM) was operated at a 15 kV accelerating voltage, 4 nA probe current, a working distance of 14 mm and a sample tilt angle of 70°. Crystal defects causing this distortion have been directly visualized using a Zeiss Merlin scanning electron microscope with a Gemini-type field emission gun electron column and a Bruker e-Flash HR-EBSD detector. The SEM was operated at 30 kV accelerating voltage, a 2–4 nA probe current and working distances between 6 and 8 mm. A theoretical introduction to ECCI as well as detailed information on sample preparation, EBSD and ECCI analyses can be found in the electronic supplementary material.

4 | RESULTS

4.1 | Sample petrography

The sample in focus shows a pinch and swell-like structure of a pyrite layer located at the margin of a sulphidized quartz vein within a mafic volcanic host rock (Figure 1a). The host rock is composed of quartz, albite, actinolite, chlorite, biotite and sulphide phases including pyrite (Figure 1). Additional quartz and calcite occur in veins and sealed cracks. The matrix consists of fine-grained quartz and albite (~20 μm) often polygonal in shape (Figure 1d), together with finely dispersed biotite defining the foliation fabric (Figure 1b).

Two pyrite types can be observed: (a) subhedral to euhedral ~200 μm porphyroblasts randomly oriented in the host rock and (b) large (0.1–1.5 cm) pyrite grains and layers associated with foliation sub-parallel veins. While the former appear undeformed, the latter are strongly fractured resulting in a puzzle-like structure built up of fragments ranging in size from 50 to 3,000 μm (Figure 1c,f). Brittle fractures are sealed by carbonates, quartz and chlorite (Figure 1b,f). Different to the matrix, vein quartz reaches grain sizes up to a few millimetres in size and shows sutured grain boundaries together with small bulges. Undulatory extinction, deformation lamellae and subgrains are common (Figure 1e).

4.2 | Brittle and crystal-plastic structures in pyrite

A variety of brittle to brittle-crystal plastic deformation structures have been observed in vein-related pyrite including: (A) minor intracrystalline distortion, (B) intracrystalline micro-cracks, which are aligned en-echelon linking up in a relay style (Peacock & Sanderson, 1995), (C) reactivated intracrystalline micro-cracks, (D) non-reactivated intracrystalline micro-cracks accompanied by a crystal-lattice rotation and a crystal-plastic zone and (E) late brittle fractures cross-cutting brittle-crystal plastic structures. Herein, we present crystal defects associated with minor intracrystalline distortion (A) and focus on three examples of structures (C) and (D) which show a clear combination of brittle and crystal-plastic deformation behaviour (Figures 2–6).

4.2.1 | (A) Intracrystalline distortion

Pyrite remote from micro-cracks shows no obvious intracrystalline deformation. The kernel average misorientation (KAM) shows a generally homogeneous pattern with no high-strain areas (Figure 2a) while minor crystal-lattice rotation can be observed in the misorientation deviation angle map (Figure 2b) as a linear misorientation gradient up to 1.5°. ECC images from similar localities show stacking faults (SFs) and a few individual dislocations (Figure 2c,d). SFs appear as planar features limited on one side by a sharp line of constant intensity (Figure 2a). Trace analysis shows that these SFs are on {001} planes (ES 3.3.1). In addition, some dot-like features show a black-and-white contrast either with the black being on the top right side and the white on the bottom left or vice versa (Figure 2c,d). These features are interpreted as dislocations with line directions sub-perpendicular to the sample surface.

4.2.2 | (C) Reactivated intracrystalline micro-cracks

Such cracks are preferentially oriented sub-parallel with foliation, having a length of up to ~100 μm. Pyrite shows a minor variation in

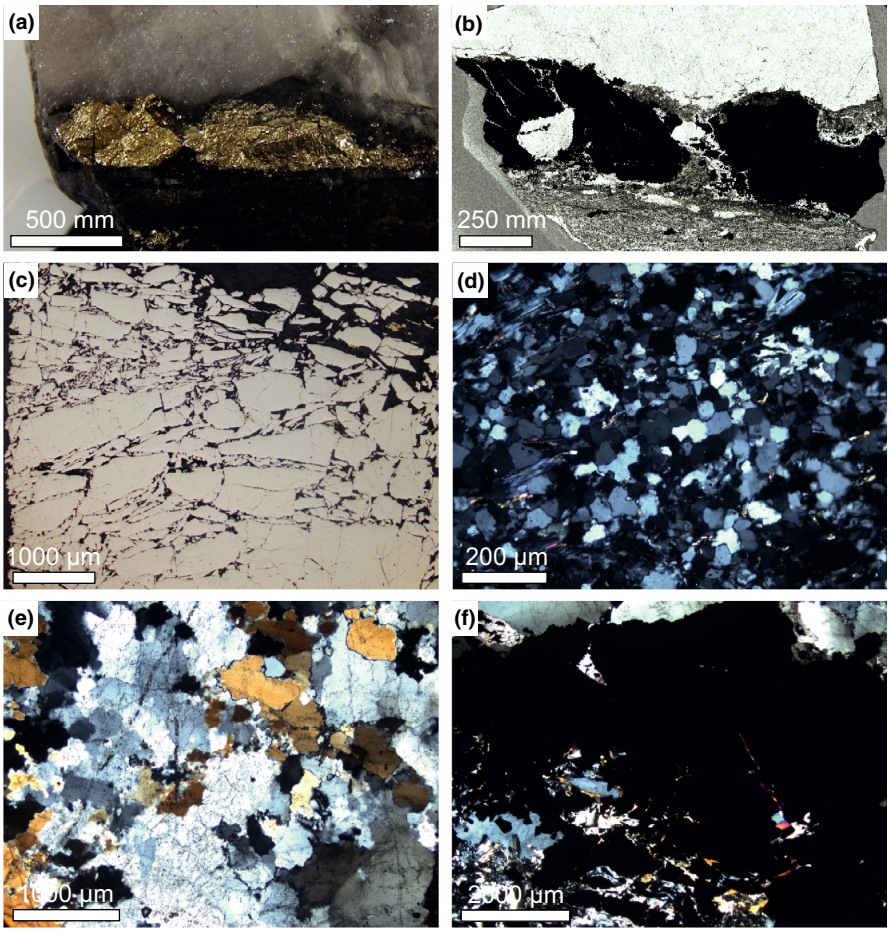

FIGURE 1 Representative images of the analysed sample. (a) Photograph of the hand specimen showing pinch and swell structure of a pyrite layer sandwiched between vein quartz and the mafic volcanic host rock. (b) Thin section scan reveals that the pyrite layer is fractured. The foliation of the host rock is traced by preferentially orientated biotite and amphibole. (c) Optical micrograph (reflected light) of intensely fractured pyrite layer. Fragments vary strongly in size and show a jigsaw-puzzle-like structure. (d) Optical micrograph (crossed polarizers) showing fine grained, almost polygonal plagioclase–quartz matrix. (e) Optical micrograph (crossed polarizers) showing coarse-grained vein quartz. Grains have abundant fluid inclusions and show undulatory extinction, sutured grain boundaries and bulges. (f) Optical micrograph (crossed polarizer) showing intensely fractured pyrite layer. Cracks are sealed by quartz, chlorite and calcite

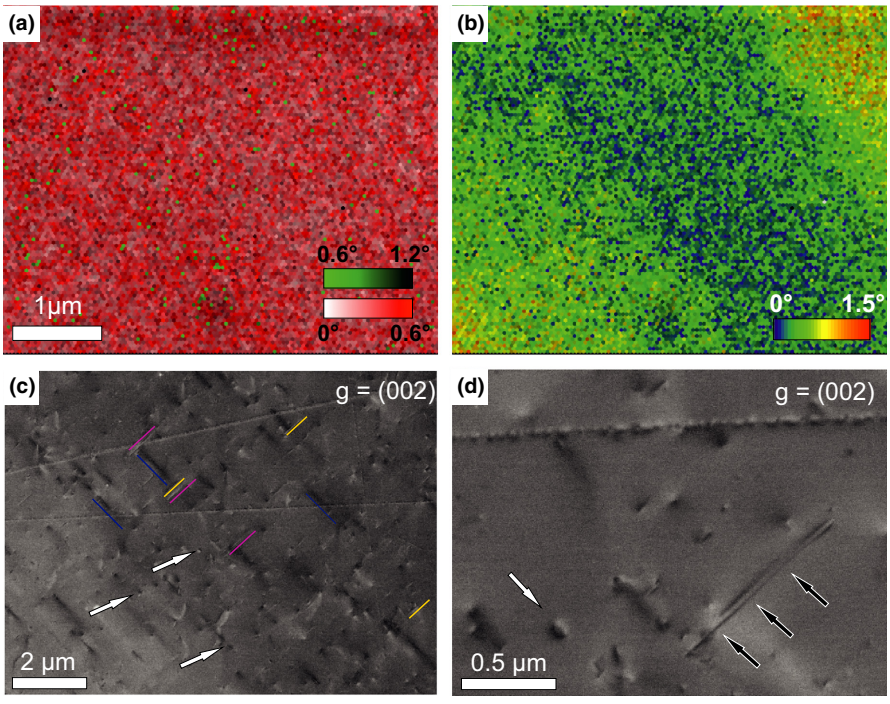

FIGURE 2 EBSD data and ECCI of pyrite remote from intracrystalline microcracks (A). (a) Combined KAM and image quality map showing a homogeneous strain distribution. (b) Misorientation deviation angle map revealing minor crystal bending by a slight colour gradient from the upper right to lower left corner of the image. (c) ECCI showing three sets of stacking faults (pink, dark blue and yellow lines) and dislocations with an orientation almost perpendicular to the sample surface (white arrows; stage tilt 13.5°). (d) High-magnification ECCI showing a stacking fault on {001} (set of black arrows) and a dislocation showing a strong black-and-white contrast on {110} (white arrow; stage tilt 13.5°)

crystal-lattice orientation on each side of the crack as seen in the misorientation deviation angle map, inverse pole figure plot (IPF) and misorientation profiles (Figure 3b,d). Misorientation starts to develop at a distance of 5 µm from the crack and increases moderately at first up to 4° before quickly jumping up at the crack locality (Figure 3d). Similar spots of increased crystal rotation can be observed

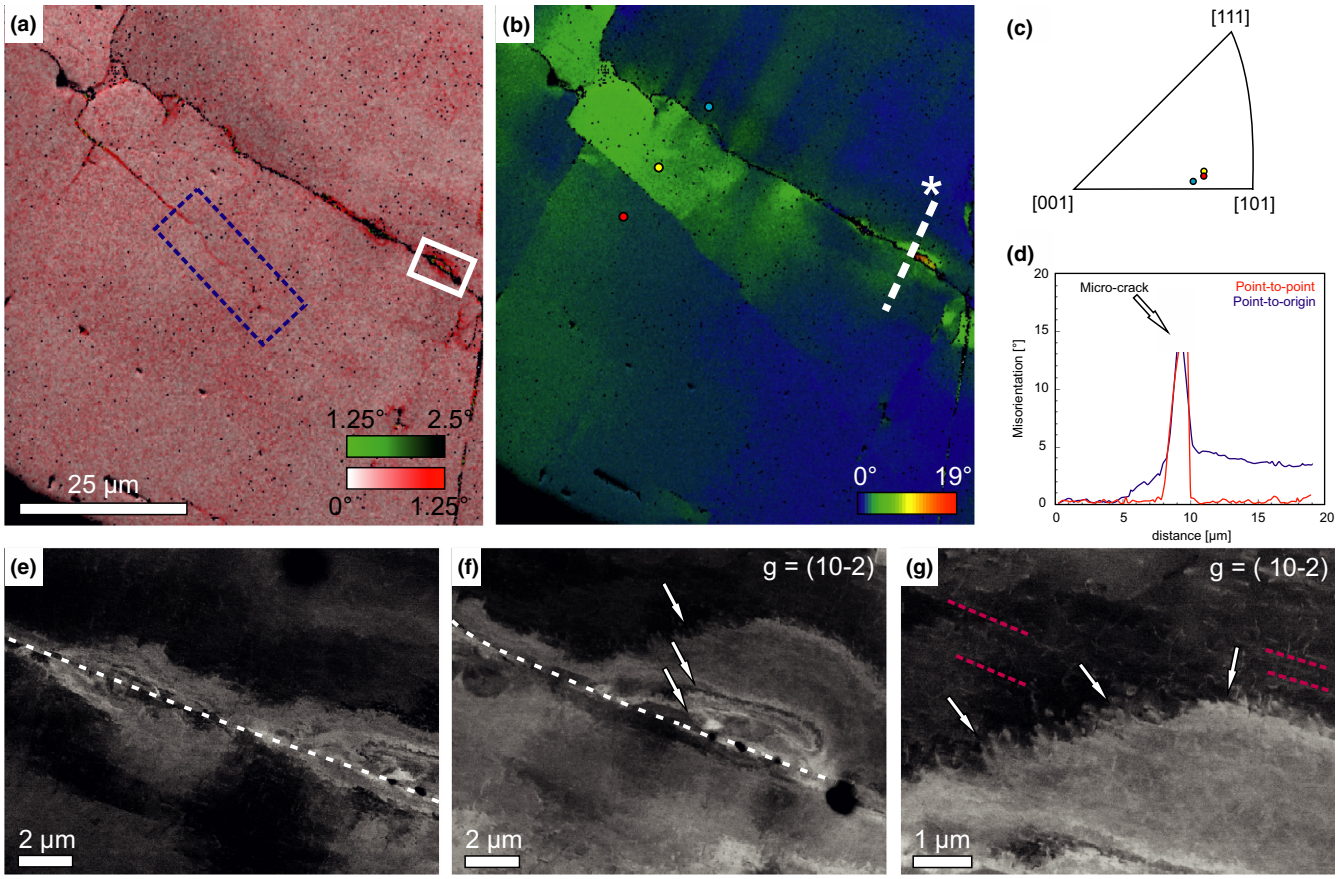

FIGURE 3 EBSD data and ECCI of reactivated intracrystalline micro-crack (B). (a) Combined KAM and image quality map. White rectangle shows locality of the ECCI in (f) and (g). Blue-dashed rectangle shows the locality of en-echelon cracks of Figure 3. (b) Misorientation deviation angle map. White-dashed line represents the locality of the misorientation profile; starting side is marked by a star. Three-coloured dots represent the localities plotted in IPF. (c) IPF of crystal orientations at different localities with respect to the micro-crack. Misorientation from blue to yellow = 5.72°; yellow to red = 1.41°. (d) Point to point (red) and point-to-origin (blue) misorientation profile orientated almost perpendicular to the micro-crack. (e) ECCI showing variation in crystal orientation along the micro-crack (white-dashed line). (f) ECCI showing increased dislocation density at the micro-crack. Note that the dislocations are arranged in zones (white arrows), increasing in size with greater distance from the crack (stage tilt 2.5°). (g) ECCI close-up of dislocation zone. Dislocations appear not well organized, curved and rather short. Slip lines are traced in pink (stage tilt 2.5°)

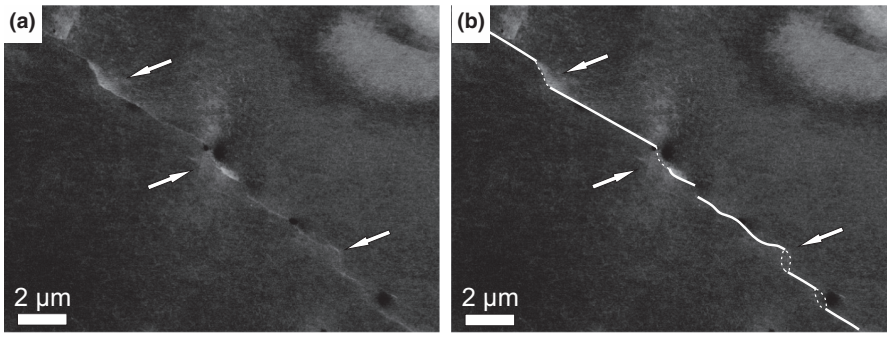

FIGURE 4 (a) ECCI image of en-echelon arranged cracks at the lower part of the reactivated intracrystalline micro-crack (B, Fig. 2). (b) White lines trace en-echelon cracks (A). White-dashed lines trace relays bridging the cracks (no stage tilt)

at several localities along the crack and are best visible in the KAM (Figure 3a) and deviation angle map (Figure 3b). In addition, a homogeneous variation in crystal bending occurs at the upper part of the micro-crack, while on the lower part en-echelon arranged cracks develop (Figures 3a,b and 4).

ECC images reveal a variation in crystal-lattice orientation associated with a grey-scale variation (Figure 3e–g). The close-up shows an increase in dislocation density in the crack vicinity consistent with the increase in lattice distortion. Dislocations are curved and appear poorly organized; nevertheless, a preferred arrangement in dislocation zones can be observed. Such arrangements result in a half-circle to elliptical bend contrast from the crack towards the crystal, cross-cutting crack-parallel slip lines tracing (010) (Figure 3g; ES 3.3.2). Localized zones of higher dislocation density are absent along en-

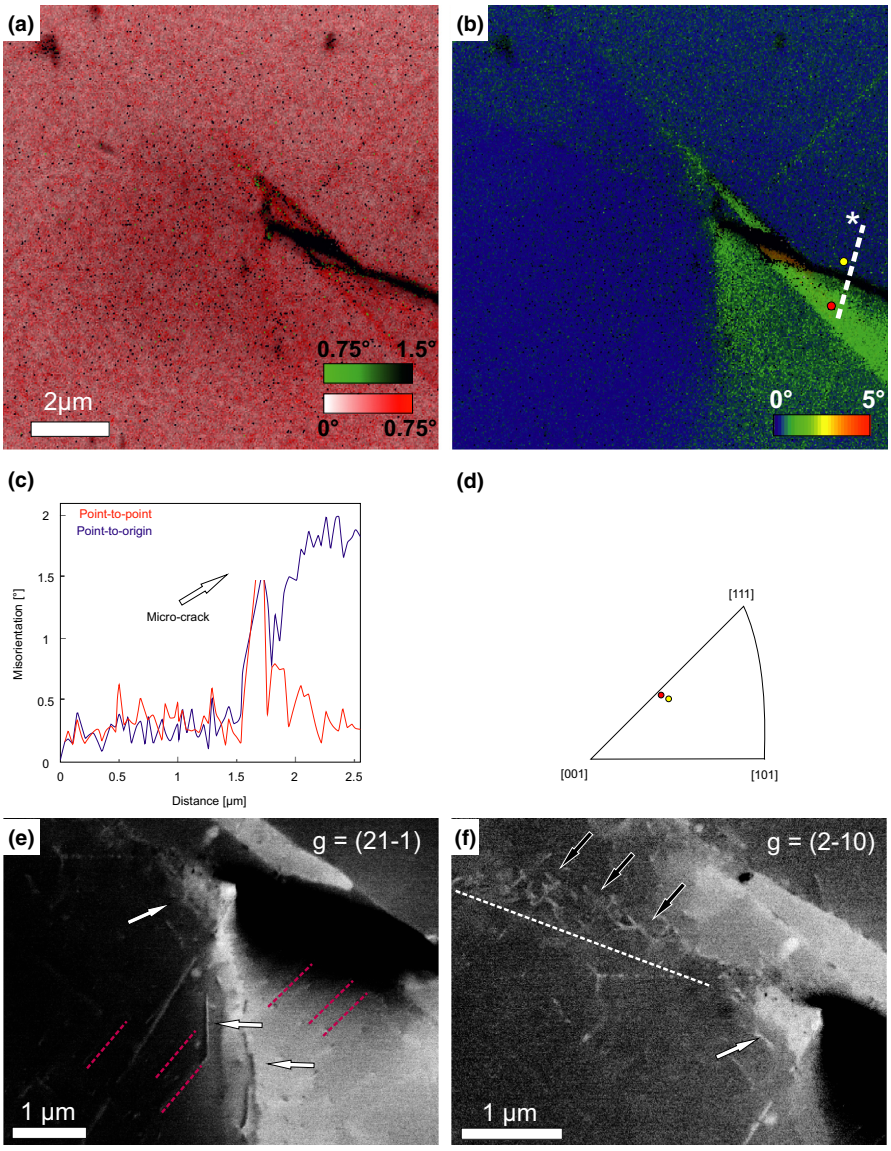

FIGURE 5 EBSD data and ECCI of non-reactivated intracrystalline micro-crack (C). (a) Combined KAM and image quality map. Note the slightly darker red colour in the vicinity of the micro-crack. (b) Misorientation deviation angle map. White-dashed line represents the locality of the misorientation profile; starting side is marked by a star. Two-coloured dots represent the localities plotted in IPF. (c) Point to point (red) and point-to-origin (blue) misorientation profile orientated almost perpendicular to the micro-crack. (d) IPF of crystal orientations at different localities with respect to the micro-crack. Misorientation from yellow to red = 1.74°. (e) ECCI of the same locality as the EBSD map in (a) and (b), showing different sets of dislocations, which appear to be emitted from the micro-crack tip (white arrows). Slip lines are traced in pink (stage tilt -0.3). (f) ECCI close-up of the micro-crack tip showing dislocations, which appear to be emitted from the micro-crack tip (arrows). Note that dislocations in the immediate vicinity of the ct are random in line direction (white arrow), while dislocations at a distance from the ct are orientated almost perpendicular to each other (black arrows) following the orientation of the micro-crack, which is indicated by the white-dashed line (stage tilt 9.4°)

echelon cracks; nevertheless ECC images show a reorientation, indicated by a variation in grey scale, preferentially located at relays (Figure 4).

4.2.3 | (D) Non-reactivated intracrystalline micro-cracks

Again, the presence of a crack is accompanied by a minor variation in crystal orientation on each side of the crack (Figure 5 and 6). In contrast to reactivated cracks, no localized zones with increased misorientation are visible; instead, we observe a slight increase in the KAM values in the crack vicinity and its tip (Figure 5a and 6a).

(D-1)

The misorientation profile shows a fairly constant crystal orientation on the upper bound of the crack, minor changes are within the error of Hough transform-based EBSD data, while on the lower bound some crystal distortion seems to occur with a misorientation of up to 2.5° (Figure 5b). At the crack tip (*ct*) and continuing the trace of the micro-crack, a minimal crystal distortion is indicated in the deviation angle map (Figure 5b). This crystal distortion is consistent with a greater number of dislocations, which seem to be emitted from the *ct*. Dislocations are arranged along the trace of the crack showing two dominant sets, running almost perpendicular to each other (black arrows in Figure 5f). Right at the *ct* no single dislocations can be identified, rather the crystal distortion is indicated by a continuous grey-scale gradient (Figure 5e,f). A second set of dislocations seems to be emitted from the *ct* with an angle of around 65° to the crack (Figure 5e). Slip lines tracing (011) are cross cut by the crack at a steep angle (Figure 5e, ES 3.3.3a).

(D-2)

Similar to the misorientation profile across the reactivated crack (Figure 3d), a continuous increase in misorientation towards the micro-crack can be observed until it quickly rises at the locality of the crack (Figure 6c). Ahead of the crack, two misorientation jumps can

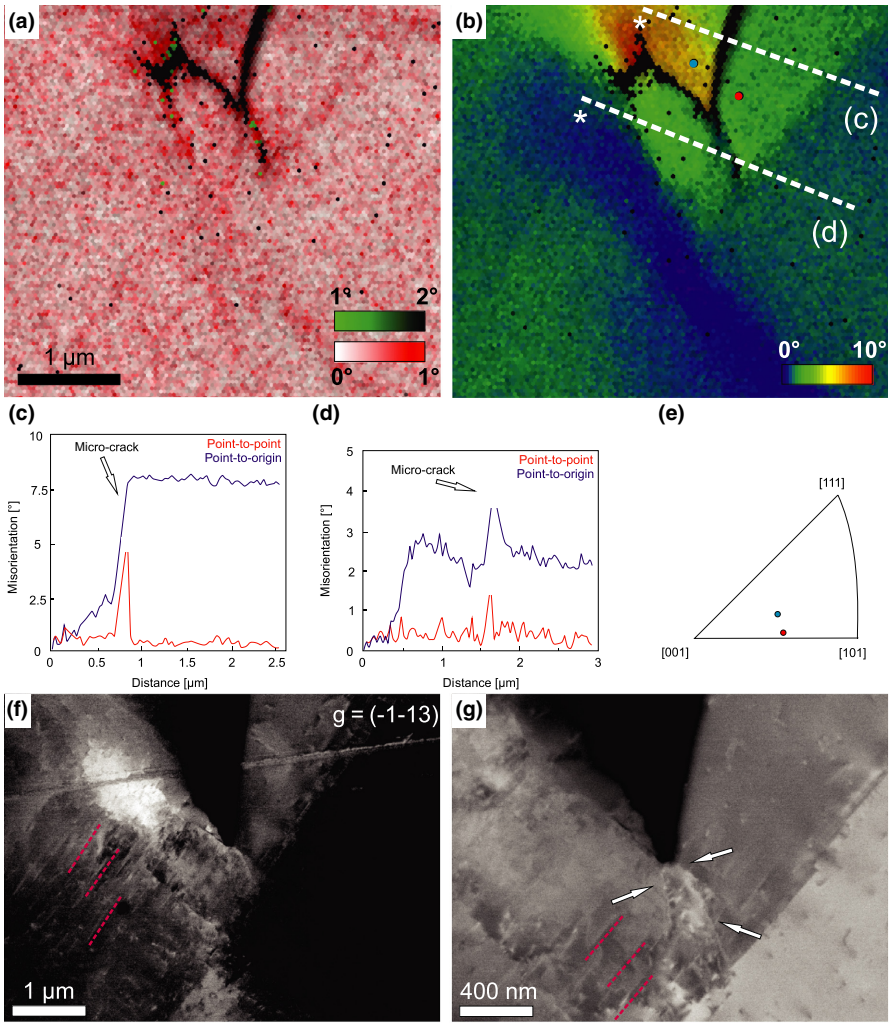

FIGURE 6 EBSD data and ECCI of non-reactivated intracrystalline micro-crack (C). (a) Combined KAM and image quality map. (b) Misorientation deviation angle map. White-dashed lines represent the localities of the misorientation profiles; starting sides are marked by a star. Two-coloured dots represent the localities plotted in IPF. (c,d) Point-to-point (red) and point-to-origin (blue) misorientation profiles. (e) IPF of crystal orientations at different localities with respect to the micro-crack. Misorientation from blue to red = 8.62°. (f) ECCI of the same locality as the EBSD map in (a) and (b), showing slip lines traced in pink (stage tilt 3.6°). (g) ECCI close-up of the micro-crack tip revealing high dislocation density at the micro-crack tip. Dislocations appear relatively straight and are emitted in various directions (stage tilt 13.5)

be observed (Figure 6d) consistent with an increased KAM at these localities (Figure 6a). ECC images reveal that these misorientation jumps align with dislocations, which are emitted from the *ct* (Figure 6g). Again, slip lines are cross cut by the crack at a high angle (Figure 6f,g).

5 | DISCUSSION AND IMPLICATIONS

5.1 | Implications for crystal defect analysis by ECCI in geological materials

Optimizing imaging conditions is essential for obtaining quality ECC images. Three conditions need to be considered: (a) the structure factor of the appropriate reflector must be high to obtain a strong signal; (b) the Bragg angle must be large enough to avoid overlap of the diffraction profiles from the diffraction vectors **g** and –**g**; and (c) the diffraction profile must not be too sharp to cope with the convergence angle of the primary beam to avoid the overlap of channelling and backscattering contrast. On pyrite only a few lattice planes, that is, "reflectors" are well suited to obtain good ECC images. The reflectors with highest structure factors are {002} 100%, {021} 69% and {022} 40%. In contrast to ECC images from metals where defects usually show a sharp white, often oscillating contrast (Zaefferer & Elhami, 2014), the defects in pyrite mostly show a distinct black–white contrast and appear blurry. Similar distinct black–white contrasts have been observed for other multi-atom crystals (Kamaladasa, Jiang, & Picard, 2011) and are likely related to the strong polarity of diffracting planes caused by the missing inversion centre of the FeS_2 symmetry group *Pa3*. The inversely contrasted dots (Figure 2c,d) likely correspond to dislocations having opposite Burgers vectors standing perpendicular to the line direction (Picard et al., 2009). Herein a possible active slip plane would be (110), with the Burgers vectors [001] and [00-1] (ES 3.3.1) being in accordance with observed slip lines (ES 3.3.3a). In geological materials, such a strong contrast in ECCI offers great possibilities as it allows for the direct detection of the Burgers vector and, therefore, of the nature of the dislocation (screw vs. edge).

5.2 | Brittle–crystal-plastic deformation of pyrite

The observed jigsaw-puzzle-like pattern of the fractured pyrite is consistent with hydraulic fracturing (Jébrak, 1997). Previously

reported cross-cutting vein types argue for several high-fluid-pressure events (Dubosq et al., 2018). While mineralization is linked to veining, fractures and cracks sealed by fluid-inclusion-rich quartz, calcite and chlorite indicate that the investigated sample has been affected by at least two increased fluid-pressure events. Fluid-assisted brecciation by hydraulic or critical fracturing (Jébrak, 1997) might have caused shattering of the strong pyrite layer within the weaker quartz–calcite-rich vein followed by quick sealing of open transgranular cracks, while intragranular micro-cracks remained open. Bulges, undulatory extinction and observed subgrains in quartz seals suggest ongoing deformation after pyrite fragmentation. While pyrite clearly deformed in a brittle manner, locally observed high dislocation densities and substructures next to micro-cracks can be associated with crystal plasticity during reactivation of cracks. The kink-like bending of the crystal lattice at the upper part of the crack (Figure 3b) together with high dislocation densities in the crack vicinity argue for accommodation of strain by crystal plasticity during micro-crack reactivation (Rawling, Baud, & Wong, 2002). In contrast, the development of en-echelon cracks and lack of crystal bending on the lower part of the crack (Figures 3 and 4) show brittle accommodation of shear strain. The co-activity of brittle and crystal-plastic behaviour during crack reactivation indicates that deformation likely occurred in the semi-brittle field (Hirth & Tullis, 1994; McLaren & Pryer, 2001). Proposed temperature conditions for brittle to ductile behaviour in pyrite vary from 260°C (Barrie, Pearce, & Boyle, 2011) to 450°C (Cox, Etheridge, & Hobbs, 1981; Graf et al., 1981). The quartz textures and occurrence of chlorite suggest reactivation took place at greenschist facies conditions within the wide range of proposed temperatures. The lack of localized dislocation zones or increased dislocation densities next to non-reactivated micro-cracks (Figure 5 and 6) indicates that the observed misorientation is related to elastic rather than plastic strain (Ohr, 1985; Pollard & Segall, 1987). Similar patterns can be observed along relay structures showing a slight lattice bending without additional dislocation activity (Figure 4). The presence of the crack seems to allow for minor reorientation and elastic bending of the crystal lattice during crack initiation (Ohr, 1985). However, stress concentration at the micro-crack tip appears to result in the emission of dislocations in the immediate vicinity of the *ct* (Figures 5e,f and 6g; Rice & Thomson, 1974). These dislocations appear random in line direction and travel between 0.5 and 2 μm deep into the crystal, indicating significant crystal plasticity at the *ct*. Furthermore, dislocations in proximity to the *ct* seem to be well arranged, following the traces of the (100) and (010) planes (Figure 5f; ES 3.3.3b) suggesting they lie within these planes. The Burgers vector cannot be determined from this one tilt experiment, yet it is evident that it is not [001] since these dislocations would be invisible with g = (2 -1 0). We argue that continuous deformation and local stress concentration at the *ct* facilitate the nucleation of dislocations, possibly supporting the onset of crystal plasticity at a later stage. A similar introduction of dislocations into the crystal lattice is likely to occur in other 'strong' minerals (Griffiths et al., 2014) but has so far been mainly reported from material sciences (Anderson, 2005; Ohr, 1985; Ugˇuz & Martin, 1996). The combination of fluid-assisted fracturing and dislocation activity is of special interest for pyrite as dislocations and substructures such as micro-cracks and low-angle grain boundaries might serve as high-diffusivity pathways (Piazolo et al., 2016; Fougerouse et al., 2018) helping to incorporate Au from hydrothermal fluids into the crystal lattice or acting as Au-traps in pyrite (Dubosq et al., 2018). The herein-observed deformation behaviour of pyrite suggests that sulphidized deposits that deformed close to the brittle–crystal-plastic transition for pyrite are likely to be highly enriched in Au.

ACKNOWLEDGEMENTS

We thank the Austrian Science Foundation (FWF) grant number: P 29539-N29 for funding. Gerlinde Habler is thanked for assistance with EBSD analysis. Discussions with Bernhard Grasemann, Michel Bestmann and David Schneider are appreciated. The manuscript benefitted from reviews by D. Fougerouse, C.D. Barrie and an anonymous reviewer. Georges Calas is thanked for careful and quick editorial handling.

ORCID

Anna Rogowitz http://orcid.org/0000-0002-6417-083X

REFERENCES

Anderson, T. L. (2005). *Fracture mechanics: fundamentals and applications* (3rd ed.). Boca Raton: CRC Press.

Barrie, C. D., Pearce, M. A., & Boyle, A. P. (2011). Reconstructing the pyrite deformation mechanism map. *Ore Geology Reviews*, *39*(4), 265–276. https://doi.org/10.1016/j.oregeorev.2011.03.006

Bleeker, W. (2015). Synorogenic gold mineralization in granite-greenstone terranes: the deep connection between extension, major faults, synorogenic clastic basins, magmatism, thrust inversion, and long-term preservation. In B. Dubé & P. Mercier-Langevin (Eds.), *Targeted Geoscience Initiative 4: Contributions to the Understanding of Precambrian Lode Gold Deposits and Implications for Exploration. Geological Survey of Canada, Open File*, *7852*, 25–47.

Boyle, A. P., Prior, D. J., Banham, M. H., & Timms, N. E. (1998). Plastic deformation of metamorphic pyrite: New evidence from electron-backscatter diffraction and forescatter orientation-contrast imaging. *Mineralium Deposita*, *34*, 71–81. https://doi.org/10.1007/s001260050186

Cox, S. F., Etheridge, M. A., & Hobbs, B. E. (1981). The experimental ductile deformation of polycrystalline and single- crystal pyrite. *Economic Geology*, *76*, 2105–2117. https://doi.org/10.2113/gsecongeo.76.8.2105

Dubosq, R., Lawley, C. J. M., Rogowitz, A., Schneider, D. A., & Jackson, S. (2018). Lithos Pyrite deformation and connections to gold mobility: Insight from micro-structural analysis and trace element mapping. *Lithos*, *310–311*, 86–104. https://doi.org/10.1016/j.lithos.2018.03.024

Fougerouse, D., Micklethwaite, S., Halfpenny, A., Reddy, S. M., Cliff, J. B., Martin, L. A. J., … Ulrich, S. (2016). The golden ark: arsenopyrite crystal plasticity and the retention of gold through high strain and metamorphism. *Terra Nova*, *28*, 181–187. https://doi.org/10.1111/ter.12206

Fougerouse, D., Reddy, S. M., Kirkland, C. L., Saxey, D. W., Rickard, D., & Hough, R. M. (2018). Time-resolved, defect-hosted, trace element mobility in deformed Witwatersrand pyrite. *Geoscience Frontiers*, 1–9. https://doi.org/10.1016/j.gsf.2018.03.010

Graf, J. L., Skinner, B. J., Bras, J., Fagot, M., Levade, C., & Couderc, J. J. (1981). Transmission electron-microscopic observation of plastic-deformation in experimentally deformed pyrite. *Economic Geology*, *76*, 738–742. https://doi.org/10.2113/gsecongeo.76.3.738

Griffiths, T. A., Habler, G., Rhede, D., Wirth, R., Ram, F., & Abart, R. (2014). Localization of submicron inclusion re-equilibration at healed fractures in host garnet. *Contributions to Mineralogy and Petrology*, *168*, 1077. https://doi.org/10.1007/s00410-014-1077-4

Hirsch, P. B., Howie, A., & Whelan, M. J. (1960). A Kinematical Theory of Diffraction Contrast of Electron Transmission Microscope Images of Dislocations and other Defects. Philosophical Transactions of the Royal Society of London. *Series A, Mathematical and Physical Sciences*, *252*, 499–529.

Hirth, G., & Tullis, J. (1994). The brittle–plastic transition in experimentally deformed quartz aggregates. *Journal of Geophysical Research*, *99*, 11731–11747. https://doi.org/10.1029/93JB02873

Jébrak, M. (1997). Hydrothermal breccias in vein-type ore deposits: A review of mechanisms, morphology and size distribution. *Ore Geology Reviews*, *12*(3), 111–134. https://doi.org/10.1016/S0169-1368(97)00009-7

Kamaladasa, R. J., Jiang, W., & Picard, Y. N. (2011). Imaging Dislocations in Single-Crystal SrTiO3 Substrates by Electron Channeling. *Journal of Electronic Materials*, *40*(11), 2222–2227.

Marmont, S. (1987). Geology of the Lower Detour Lake-Hopper-Sunday Lakes area, northeastern Ontario. *Ontario Geological Survey. Miscellaneous Paper*, *137*, 175–180.

McLaren, A. C., & Pryer, L. L. (2001). Microstructural investigation of the interaction and interdependence of cataclastic and plastic mechanisms in Feldspar crystals deformed in the semi-brittle field. *Tectonophysics*, *335*(1–2), 1–15. https://doi.org/10.1016/S0040-1951(01)00042-7

Miyajima, N., Abeykoon, S., & Heidelbach, F. (2018). Electron channelling contrast imaging of individual dislocations in geological materials using a field-emission scanning electron microscope equipped with an EBSD system. *European Journal of Mineralogy*, *30*, 5–15. https://doi.org/10.1127/ejm/2017/0029-2683

Ohr, S. M. (1985). An electron microscope study of crack tip deformation and its impact on the dislocation theory of fracture. *Materials Science and Engineering*, *72*(1), 1–35. https://doi.org/10.1016/0025-5416(85)90064-3

Oliver, J., Ayer, J., Dubé, B., Aubertin, R., Burson, M., Panneton, G., … Hamilton, M. (2011). Structure, stratigraphy, U-Pb geochronology and alteration characteristics of gold mineralization at the Detour Lake deposit, Ontario, Canada. *Exploration and Mining Geology*, *20*, 1–30.

Peacock, D. C. P., & Sanderson, D. J. (1995). Strike-slip relay ramps. *Journal of Structural Geology*, *17*(10), 1351–1360. https://doi.org/10.1016/0191-8141(95)97303-W

Piazolo, S., La Fontaine, A., Trimby, P., Harley, S., Yang, L., Armstrong, R., & Cairney, J. M. (2016). Deformation-induced trace element redistribution in zircon revealed using atom probe tomography. *Nature Communications*, *7*, 10490. https://doi.org/10.1038/ncomms10490

Picard, Y. N., Twigg, M. E., Caldwell, J. D., Eddy, C. R., Mastro, M. A., & Holm, R. T. (2009). Resolving the Burgers vector for individual GaN dislocations by electron channeling contrast imaging. *Scripta Materialia*, *61*, 773–776. https://doi.org/10.1016/j.scriptamat.2009.06.021

Pollard, D. D., & Segall, P. (1987). Theoretical displacements and stresses near fractures in rock: with applications to faults, joints, veins, dikes, and solution surfaces. In B. Atkinson (Ed.), *Fracture Mechanics of Rock* (pp. 277–349). Orlando: Academic Press. https://doi.org/10.1016/B978-0-12-066266-1.50013-2

Rawling, G. C., Baud, P., & Wong, T. (2002). Dilatancy, brittle strength, and anisotropy of foliated rocks: Experimental deformation and micromechanical modeling. *Journal of Geophysical Research: Solid Earth*, *107*(B10), ETG 8-1–ETG 8-14. https://doi.org/10.1029/2001jb000472

Rice, J. R., & Thomson, R. (1974). Ductile versus brittle behaviour of crystals. *Philosophical Magazine*, *29*(1), 73–97. https://doi.org/10.1080/14786437408213555

Ugˇuz, A., & Martin, J. W. (1996). Plastic zone size measurement techniques for metallic materials. *Materials Characterization*, *37*(2), 105–118. https://doi.org/10.1016/S1044-5803(96)00074-5

Wallis, D., Parsons, A. J., & Hansen, L. N. (2017). Quantifying geometrically necessary dislocations in quartz using HR-EBSD: Application to chessboard subgrain boundaries. *Journal of Structural Geology*, (December), 0–1. https://doi.org/10.1016/j.jsg.2017.12.012

Wheeler, J., Mariani, E., Piazolo, S., Prior, D. J., Trimby, P., & Drury, M. R. (2009). The weighted Burgers vector: A new quantity for constraining dislocation densities and types using electron backscatter diffraction on 2D sections through crystalline materials. *Journal of Microscopy*, *233*(3), 482–494. https://doi.org/10.1111/j.1365-2818.2009.03136.x

Zaefferer, S., & Elhami, N. N. (2014). Theory and application of electron channelling contrast imaging under controlled diffraction conditions. *Acta Materialia*, *75*(154), 20–50. https://doi.org/10.1016/j.actamat.2014.04.018

SUPPORTING INFORMATION

Additional supporting information may be found online in the Supporting Information section at the end of the article.

Data S1. Additional information on methodology (EBSD, ECCI and dislocation trace analysis).

Data S2. Figures.

How to cite this article: Rogowitz A, Zaefferer S, Dubosq R. Direct observation of dislocation nucleation in pyrite using combined electron channelling contrast imaging and electron backscatter diffraction. *Terra Nova*. 2018;30:423–430. https://doi.org/10.1111/ter.12358